THE UNIVERSITY of EDINBURGH

Edinburgh Research Explorer

Large Eddy Simulation of turbulent nonpremixed sooting flames: Presumed subfilter PDF model for finite-rate oxidation of soot

Citation for published version:
Colmán, HM, Attili, A & Mueller, ME 2023, 'Large Eddy Simulation of turbulent nonpremixed sooting flames: Presumed subfilter PDF model for finite-rate oxidation of soot', *Combustion and Flame*. https://doi.org/10.1016/j.combustflame.2022.112602

Digital Object Identifier (DOI):
10.1016/j.combustflame.2022.112602

Link:
Link to publication record in Edinburgh Research Explorer

Document Version:
Peer reviewed version

Published In:
Combustion and Flame

General rights
Copyright for the publications made accessible via the Edinburgh Research Explorer is retained by the author(s) and / or other copyright owners and it is a condition of accessing these publications that users recognise and abide by the legal requirements associated with these rights.

Take down policy
The University of Edinburgh has made every reasonable effort to ensure that Edinburgh Research Explorer content complies with UK legislation. If you believe that the public display of this file breaches copyright please contact openaccess@ed.ac.uk providing details, and we will remove access to the work immediately and investigate your claim.

OPEN ACCESS

Download date: 13. Jan. 2023

Manuscript Click here to view linked References

Large Eddy Simulation of turbulent nonpremixed sooting flames: Presumed subfilter PDF model for finite-rate oxidation of soot

Hernando Maldonado Colmán[a,*], Antonio Attili[b], Michael E. Mueller[a]

[a] *Department of Mechanical and Aerospace Engineering, Princeton University, Princeton, NJ 08544, USA*

[b] *Institute for Multiscale Thermofluids, School of Engineering, University of Edinburgh, Edinburgh, EH9 3FD, United Kingdom*

Abstract

Modeling soot evolution in turbulent reacting flows using Large Eddy Simulation (LES) is challenging due to the complex subfilter soot-turbulence-chemistry interactions. Soot particles form at fuel-rich mixtures and are subsequently oxidized as they are transported toward fuel-lean mixtures. In previous work, this phenomenology was explicitly encoded into a presumed subfilter PDF model for soot by confining soot strictly to mixtures where growth rates exceed oxidation rates. However, this model implicitly assumed that oxidation is infinitely fast. In this work, a new presumed subfilter PDF model for soot is proposed to account for finite-rate soot oxidation. The distribution of soot with respect to the flame structure (mixture fraction) is modeled by comparing the local relative motion of diffusionless soot particles with respect to mixture fraction iso-contours with the local oxidation rate. When the oxidation rate is suppressed or the transport rate is very fast, soot

*Corresponding author.
Email address: hm2524@princeton.edu (Hernando Maldonado Colmán)

is allowed to penetrate further into fuel-lean mixtures. This model can allow for soot leakage across the flame, a critical phenomenon in smoking flames. The new model is validated *a priori* against Direct Numerical Simulation (DNS) databases of turbulent nonpremixed jet flames and then *a posteriori* against experimental measurements in a laboratory-scale turbulent jet flame. *A priori* results show remarkably good agreement with filtered DNS data and are shown to correctly allow for soot leakage at low Damköhler number. Finally, LES results of the turbulent sooting jet flame show an improvement of soot prediction using the new soot subfilter model compared to previous works. In this flame, as in experiments, evidence of soot leakage is found near the beginning of the sooting region, and this soot leakage cannot be predicted with previous subfilter models that presume infinitely fast oxidation.
Keywords:
Soot; Soot-turbulence-chemistry interactions; Soot oxidation; Large Eddy Simulation (LES); Presumed subfilter PDF

---

1. Introduction

Among the various computational modeling challenges of turbulent sooting flames, small-scale soot-turbulence-chemistry interactions is one of the most difficult. Soot particles are characterized by very small to null diffusion in the turbulent reacting flow and very slow chemical pathways in their formation [1], leading to ligament-like soot particle-laden structures stretched by the turbulent vortices [2, 3]. This results in significant soot intermittency, both temporally and spatially, at unresolved scales [4]. Therefore, considerable modeling efforts are needed to provide closure for Large Eddy Simulation

(LES).

A few attempts have been made to reproduce the high intermittency of soot at unresolved LES subfilter scales, where the subfilter intermittency is defined by Mueller and Pitsch [4] as the probability of not finding soot within the filter volume. In that work [4], to capture this subfilter intermittency, a presumed subfilter PDF model for LES, which represents the statistical distribution of scalar moments of the soot number density function and accounts for turbulence-soot-chemistry interactions, was first introduced. In the model, the subfilter PDF was divided into a non-sooting mode and a sooting mode, each represented by delta functions, weighted by the subfilter intermittency. In this first model, the probability of finding soot was uncorrelated with the thermochemical state since soot phenomena were explicitly presumed to be slower than the gas-phase chemistry [4]. This soot subfilter PDF model was applied in several turbulent combustion configurations [5–9].

The soot subfilter PDF model of Mueller and Pitsch [4] has been improved in two ways. Berger *et al.* [10] reformulated the sooting mode to be a lognormal distribution and, in an *a priori* analysis, found an improvement of the prediction of the filtered coagulation source term. On the other hand, Yang *et al.* [11] focused on formulating a correlation with the flame structure (mixture fraction) and argued that soot phenomena occur at a wide range of timescales. Specifically, soot oxidation can take place at similar timescales as the combustion processes. Therefore, Yang *et al.* [11] developed a conditional soot subfilter PDF confining soot to fuel-rich regions where soot surface growth is faster than soot oxidation. This conditional PDF model was shown to dramatically improve predictions of soot oxidation (by eliminating "spu-

rious" oxidation). However, due to its form, this conditional soot subfilter PDF model implicitly assumes that oxidation is infinitely fast compared to turbulent transport of soot.

The assumption of infinitely fast oxidation is not universally true. Soot can leak into lean mixtures unoxidized in what are generally referred to as smoking flames. The most common mechanism of smoking flames is the suppression of oxidation rates due to a reduction in temperature by radiation heat losses in flames with long residence times and large Damköhler numbers (see, *e.g.*, Ref. [12]). A second mechanism was proposed from computational observations by Attili *et al.* [13, 14] in a three-dimensional DNS of an *n*-heptane/nitrogen fueled non-premixed flame in the small Damköhler number regime, when local extinction arises so soot oxidation is suppressed. A model that assumes infinitely fast oxidation would not be able to capture these finite-rate oxidation phenomena.

In this work, a new presumed subfilter PDF model to capture finite-rate oxidation of soot particles in a turbulent reacting flow is proposed and is implemented in an LES framework based on state-of-the-art combustion and soot models [15, 16]. The new model accounts for the local relative motion of diffusionless soot particles relative to the mixture fraction iso-contour, given by the mixture fraction displacement speed, which scales with the local mixture fraction dissipation rate, and compares it against the local oxidation rate, determining a new soot distribution with respect to the mixture fraction. The finite-rate oxidation model is assessed *a priori* using the DNS data from Attili *et al.* [14] at different Damköhler numbers and then evaluated *a posteriori* in a turbulent nonpremixed jet flame [17].

This paper is structured as follows. The fundamentals of LES modeling for turbulent combustion including soot evolution are introduced in Section 2. Subfilter models to capture soot-turbulence-chemistry interactions are presented in Section 3, including the considerations of the new presumed soot subfilter PDF models as well as previous works. In Section 4, the new soot subfilter PDF model is validated *a priori* using DNS data and compared against previous models. Finally, an extensive *a posteriori* validation is made in Section 5, by comparing computational results using the new and previous models to experimental data in a laboratory-scale turbulent sooting flame.

2. LES modeling framework

The purpose of this section is to present the governing equations and models involved in the LES framework for soot evolution in turbulent reacting flows.

2.1. Soot model

A Number Density Function (NDF) statistically represents the soot particles classified by size, and the Population Balance Equation (PBE) describes the evolution of the NDF in time, space, and internal (size) variables. In this work, a bivariate NDF is considered, with internal variables soot particle volume V and soot particle surface area S [18]. The PBE is computationally expensive to solve, especially using multivariate NDFs. Instead, the method of moments is used in which the evolution of the NDF is described by transporting instead a few statistical moments $M_{x,y}$. For the bivariate NDF, the

soot statistical moment is defined as

$$M_{x,y} = \sum_{\eta=1}^{\infty} V_\eta^x S_\eta^y N_\eta, \tag{1}$$

where N_η is the particle number density in the two-dimensional state space element η, corresponding to the particle "class" of volume V_η and surface area S_η. The subscripts x and y indicate the order of the moment regarding the soot size parameters V and S, respectively. The moments $M_{0,0}$, $M_{1,0}$, and $M_{0,1}$ have a physical meaning corresponding to the soot number density, the soot volume fraction, and the total soot surface, respectively. The moment transport equations require closure for the moment source terms $\dot{M}_{x,y}$ since they are not directly evaluated using the moments $M_{x,y}$. The Hybrid Method of Moments (HMOM) provide closures for these source terms describing different soot phenomena, such as nucleation, coagulation, condensation, surface growth, oxidation, and oxidation-induced fragmentation. HMOM has been extensively validated in numerous laminar flames [15, 18, 19]. HMOM accounts for the bimodality of the NDF by transporting a supplementary weighted delta function that mimics the number density of nascent soot particles N_0.

The soot moments $M_{x,y}$ and the incipient particles N_0 are denoted by the soot scalar M_j and are governed by the transport equation:

$$\frac{\partial M_j}{\partial t} + \frac{\partial u_i^* M_j}{\partial x_i} = \dot{M}_j, \tag{2}$$

where u_i^* stands for the total velocity of soot particles (flow and thermophoresis) and $\dot{M}_j$ are the soot scalar source terms. The latter is decomposed in the different soot phenomena described above.

2.2. Combustion model

In this work, combustion is modeled using the Radiation Flamelet/Progress Variable (RFPV) model for non-adiabatic nonpremixed combustion [16, 20], where the computations of the flow field and the detailed flame structure are decoupled. A set of parameters–composed of mixture fraction Z, progress variable C, and heat loss parameter H–describes the flame structure and establishes a thermochemical database accessible by the LES solver.

The governing equations for Z, C, and H are written as follows:

$$\frac{\partial \rho Z}{\partial t} + \frac{\partial \rho u_i Z}{\partial x_i} = \frac{\partial}{\partial x_i}\left(\rho D_Z \frac{\partial Z}{\partial x_i}\right) + \dot{m}_Z, \tag{3}$$

$$\frac{\partial \rho C}{\partial t} + \frac{\partial \rho u_i C}{\partial x_i} = \frac{\partial}{\partial x_i}\left(\rho D_C \frac{\partial C}{\partial x_i}\right) + \dot{m}_C, \tag{4}$$

$$\frac{\partial \rho H}{\partial t} + \frac{\partial \rho u_i H}{\partial x_i} = \frac{\partial}{\partial x_i}\left(\rho D_H \frac{\partial H}{\partial x_i}\right) + \dot{\rho} H + \dot{q}_{\mathrm{RAD}}. \tag{5}$$

The mixture fraction Z requires a source term $\dot{m}_Z$ to account for the consumption of PAH species to produce soot; the progress variable C has a source term $\dot{m}_C$ that is rescaled from for the change in the effective stoichiometry because of the large C/H ratio of PAH species removed from the gas mixture; and the heat loss parameter H is zero-valued for adiabatic conditions [16]. $\dot{q}_{\mathrm{RAD}}$ indicates the radiative source term and considers the gas-phase optically thin gray model from Barlow *et al.* [21], which accounts for the species CO_2, H_2O, CO, and CH_4, and the soot radiation model is from Hubbard and Tien [22].

PAH chemistry has a much slower characteristic time scale compared to the major combustion products. To incorporate this feature, special attention is taken to the flow history dependence [23] so slow adjustment to fluctuating scalar dissipation rates [24] that characterize PAH evolution, so an explicit transport equation is written as [16]

$$\frac{\partial \rho Y_{\mathrm{PAH}}}{\partial t} + \frac{\partial \rho u_i Y_{\mathrm{PAH}}}{\partial x_i} = \frac{\partial}{\partial x_i}\left(\rho D_{\mathrm{PAH}} \frac{\partial Y_{\mathrm{PAH}}}{\partial x_i}\right) + \dot{m}_{\mathrm{PAH}}, \tag{6}$$

where $\dot{m}_{\mathrm{PAH}}$ is the summation of PAH species source terms. The PAH source term is formulated following the work of Mueller and Pitsch [16]. For species with slow chemistry (*e.g.*, PAHs) confined in zones of small scalar dissipation rates, a strain-sensitive transport approach (SSTA) is utilized [25]. Molecular Lewis numbers are considered for the species where molecular transport dominates. However, fast chemistry species hold the unity Lewis number assumption [24].

2.3. LES governing equations

The LES filtered scalar transport equations are obtained after a filtering operation is applied to Eqs. 2-6 and gives the following system:

$$\frac{\partial \overline{\rho}\widetilde{Z}}{\partial t} + \frac{\partial \overline{\rho}\widetilde{u}_i\widetilde{Z}}{\partial x_i} = \frac{\partial}{\partial x_i}\left(\overline{\rho}\widetilde{u}_i\widetilde{Z} - \overline{\rho}\widetilde{u_i Z}\right) + \frac{\partial}{\partial x_i}\left(\overline{\rho}\widetilde{D}_Z \frac{\partial \widetilde{Z}}{\partial x_i}\right) + \overline{\dot{m}}_Z, \tag{7}$$

$$\frac{\partial \overline{\rho}\widetilde{C}}{\partial t} + \frac{\partial \overline{\rho}\widetilde{u}_i\widetilde{C}}{\partial x_i} = \frac{\partial}{\partial x_i}\left(\overline{\rho}\widetilde{u}_i\widetilde{C} - \overline{\rho}\widetilde{u_i C}\right) + \frac{\partial}{\partial x_i}\left(\overline{\rho}\widetilde{D}_C \frac{\partial \widetilde{C}}{\partial x_i}\right) + \overline{\dot{m}}_C, \tag{8}$$

$$\begin{aligned}\frac{\partial \overline{\rho}\widetilde{H}}{\partial t} + \frac{\partial \overline{\rho}\widetilde{u}_i\widetilde{H}}{\partial x_i} = &\frac{\partial}{\partial x_i}\left(\overline{\rho}\widetilde{u}_i\widetilde{H} - \overline{\rho}\widetilde{u_i H}\right) \\ &+ \frac{\partial}{\partial x_i}\left(\overline{\rho}\widetilde{D}_H \frac{\partial \widetilde{H}}{\partial x_i}\right) + \overline{\dot{\rho} H} + \overline{\dot{q}}_{\mathrm{RAD}},\end{aligned} \tag{9}$$

$$\frac{\partial \overline{\rho}\widetilde{Y}_{\mathrm{PAH}}}{\partial t} + \frac{\partial \overline{\rho}\widetilde{u}_i\widetilde{Y}_{\mathrm{PAH}}}{\partial x_i} = \frac{\partial}{\partial x_i}\left(\overline{\rho}\widetilde{u}_i\widetilde{Y}_{\mathrm{PAH}} - \overline{\rho}\widetilde{u_i Y}_{\mathrm{PAH}}\right) + \frac{\partial}{\partial x_i}\left(\overline{\rho}\widetilde{D}_{\mathrm{PAH}}\frac{\partial \widetilde{\mathrm{Y}}_{\mathrm{PAH}}}{\partial x_i}\right) + \overline{\dot{m}}_{\mathrm{PAH}}, \tag{10}$$

$$\frac{\partial \overline{M}_j}{\partial t} + \frac{\partial \widetilde{u_i}^*\overline{M}_j}{\partial x_i} = \frac{\partial}{\partial x_i}\left(\widetilde{u}_i^*\overline{M}_j - \overline{u_i^* M_j}\right) + \overline{\dot{M}}_j, \tag{11}$$

where $\overline{\varphi}$ and $\widetilde{\varphi}$ indicates the filtering and density-weighted filtering operations applied to a variable φ, respectively. In the right-hand side of every equation, the first term is the subfilter scalar flux and describes the unresolved turbulent transport; the second term, except for the soot scalars because of the negligible soot diffusion assumption, is the filtered molecular diffusion flux; and the final terms are the filtered source terms. The unresolved terms comprise the small-scale unresolved soot-turbulence-chemistry interactions, and closure models are presented in the following section. The closure for the filtered PAH source term developed by Mueller and Pitsch [16] is utilized in this work.

3. Subfilter modeling for turbulence-chemistry-soot interactions

Small-scale unresolved soot-turbulence-chemistry interactions can be modeled in LES by closing the filtered source terms $\overline{\dot{Q}}$ through a convolution against a density-weighted joint subfilter PDF $\widetilde{P}(\xi_k, M_j)$, which depends on the thermochemical variables ξ_k and soot scalars M_j:

$$\overline{\dot{Q}}(\xi_k, M_j) = \overline{\rho}\iint \frac{1}{\rho}\dot{Q}(\xi_k, M_j)\widetilde{P}(\xi_k, M_j)d\xi_k dM_j, \tag{12}$$

where the subfilter PDF $\widetilde{P}(\xi_k, M_j)$ needs to be modeled. By Bayes' theorem, the subfilter PDF can be written as

$$\widetilde{P}(\xi_k, M_j) = \widetilde{P}(\xi_k)\widetilde{P}(M_j \mid \xi_k), \tag{13}$$

where $\widetilde{P}(\xi_k)$ is modeled as a beta distribution for the mixture fraction $\widetilde{P}(Z) = \beta(Z, \widetilde{Z}(x_j), Z_v(x_j))$ [20, 26], where $\widetilde{Z}(x_j)$ and $Z_v(x_j) = \widetilde{Z^2}(x_j) - \widetilde{Z}^2(x_j)$ are the local filtered and subfilter variance of the mixture fraction, respectively. Another transport equation is therefore solved for filtered $\widetilde{Z^2}$ [16], in addition to Eqs. 7–11, in order to compute the subfilter mixture fraction variance Z_v, which is also included in the RFPV database, for the computation of such presumed subfilter PDFs of Eqs. 12–13. The conditional soot subfilter PDF $\widetilde{P}(M_j \mid \xi_k)$ is discussed in the following subsection.

3.1. Previous models

Mueller and Pitsch [4] modeled a presumed subfilter PDF for soot-turbulence interactions as a highly intermittent (at the subfilter level) bimodal PDF with two states corresponding to sooting $\widetilde{P}_S$ and non-sooting $\widetilde{P}_{NS}$ modes, written as

$$\widetilde{P}(M_j \mid \xi_k) = \omega\widetilde{P}_{NS} + (1-\omega)\widetilde{P}_S, \tag{14}$$

where ω is the soot subfilter intermittency and represents the probability of not finding soot at the subfilter scale. Mueller and Pitsch [4] argued that the characteristic time scales of soot were slower than the heat releasing combustion chemistry so the subfilter PDF model could be considered as independent of the thermochemical variables $\widetilde{P}(M_j \mid \xi_k) = \widetilde{P}(M_j)$. Furthermore, since soot is highly intermittent, delta functions were considered to

construct the bimodal distribution, where the non-sooting mode is

$$\widetilde{P}_{NS} = \delta(M_j) \tag{15}$$

and the sooting mode is

$$\widetilde{P}_{S} = \delta(M_j - M_j^*). \tag{16}$$

This model is referred to as the marginal (Marg) model. The subfilter intermittency depends on a second-order moment. For the marginal model, the subfilter intermittency is written as [4]

$$\omega = 1 - \frac{\overline{M}_j^2}{\overline{M_j^2}}. \tag{17}$$

The best quantity to model the subfilter intermittency is $M_{0,0}$ (total number density), and a transport equation must then be solved for the second-order moment $\overline{M_{0,0}^2}$ [4]. M_j^* are chosen such that $\overline{M}_j$ are obtained upon convolution against $\widetilde{P}(\xi_k, M_j)$ as follows:

$$\begin{aligned} \overline{M}_j &= \iint M_j P\left(M_j \mid \xi_k\right) \widetilde{P}\left(\xi_k\right) d\xi_k dM_j \\ &= (1-\omega) M_j^* \int \widetilde{P}\left(Z\right) dZ \\ &= \frac{\overline{M}_{0,0}^2}{\overline{M_{0,0}^2}} M_j^*. \end{aligned} \tag{18}$$

Therefore, M_j^* in terms of the filtered soot scalars is

$$M_j^* = \frac{\overline{M}_j}{1-\omega} \tag{19}$$

To determine the filtered source terms, first note that the soot scalar source terms for oxidation (ox) and surface growth (sg) can be written as

the product of the oxidation or growth rate coefficients and a function of the moments:

$$\dot{M}_j^{\mathrm{ox/sg}} = k_{\mathrm{ox/sg}}(\xi_k) f(M_j). \tag{20}$$

Then, the filtered source terms for oxidation and surface growth are obtained from convolution against the joint subfilter PDF:

$$\overline{\dot{M}_j}^{\mathrm{ox/sg}} = \iint k_{\mathrm{ox/sg}}\left(\xi_k\right) f\left(M_j\right) P\left(M_j \mid \xi_k\right) \widetilde{P}\left(\xi_k\right) d\xi_k dM_j. \tag{21}$$

Evaluating Eq. 21 with the Marg model gives

$$\overline{\dot{M}_j}^{\mathrm{ox/sg}} = \widetilde{k}_{\mathrm{ox/sg}} \left[\frac{\overline{M}_{0,0}^2}{\overline{M_{0,0}^2}} f\left(M_j^*\right) \right], \tag{22}$$

where $\widetilde{k}_{\mathrm{ox/sg}}$ is the density-weighted filtered rate coefficient.

Later, Yang *et al.* [11] attempted to model the conditional soot subfilter PDF. The authors considered that soot is confined to subfilter mixtures where growth rates exceed oxidation rates, and, at the same time, competitive with gas-phase chemistry time scales but very fast compared to other soot processes. Therefore, they considered a presumed subfilter PDF for the sooting mode that depends on the mixture fraction Z as

$$\widetilde{P}_S = \delta\left(M_j - M_j^*(Z, \chi_{st})\right), \tag{23}$$

where $M_j^*(Z, \chi_{st}) = M_j^{**} H(Z, \chi_{\mathrm{st}})$ and M_j^{**} are chosen such that $\overline{M}_j$ is recovered upon convolution against $\widetilde{P}(\xi_k)$. $H(Z, \chi_{\mathrm{st}}) = H(Z - Z_{\mathrm{soot}}(\chi_{\mathrm{st}}))$ is the Heaviside function, and Z_{soot} is the mixture fraction value at which the soot surface growth is equal to the rate of soot oxidation. This Z_{soot} varies with the mixture fraction dissipation rate (reference at stoichiometric mixture

fraction) χ_{st}. With the Heaviside function, this model actually implicitly assumes that soot oxidation is infinitely fast. Hereafter, this model from Yang *et al.* [11] will be referred to as the Infinitely Fast Oxidation (IFO) model.

The IFO model requires a modification of the subfilter intermittency in Eq. 17 to recover the filtered soot scalars upon convolution:

$$\omega = 1 - \frac{1}{\int H(Z - Z_{\mathrm{soot}})\widetilde{P}(Z)dZ} \cdot \frac{\overline{M}_{0,0}^2}{\overline{M_{0,0}^2}}, \tag{24}$$

where $\widetilde{P}(Z)$ is the beta distribution as stated before. Then, analogously to Eqs. 18-19, the expression for $M_j^{**}(Z)$ after some algebraic manipulation is written as

$$M_j^{**} = \frac{\overline{M}_j}{(1-\omega)\int H(Z - Z_{\mathrm{soot}})\widetilde{P}(Z)dZ}. \tag{25}$$

Yang *et al.* [11] showed that the filtered source terms for oxidation and surface growth for the IFO model can be expressed as

$$\overline{\dot{M}}_j^{\mathrm{ox/sg}} = \check{k}_{\mathrm{ox/sg}} \left[\frac{\overline{M}_{0,0}^2}{\overline{M_{0,0}^2}} f\left(M_j^{**}\right) \right], \tag{26}$$

where $\check{k}_{\mathrm{ox/sg}}$ is the rate coefficient convoluted against the thermochemical PDF weighted by the Heaviside function:

$$\check{k}_{\mathrm{ox/sg}} = \left[\frac{\int k_{\mathrm{ox/sg}}\left(\xi_k\right) H\left(Z - Z_{\mathrm{soot}}\right) \widetilde{P}\left(\xi_k\right) d\xi_k}{\int H\left(Z - Z_{\mathrm{soot}}\right) \widetilde{P}\left(\xi_k\right) d\xi_k} \right]. \tag{27}$$

All quantities in Eqs. 22,26-27 are functions of Z and χ_{st} (via Z_{soot}) and can be precomputed and stored in a precomputed database [11].

3.2. Soot subfilter PDF for finite-rate oxidation

While the assumption of infinitely fast oxidation is valid under some conditions, the assumption is not valid under all conditions. The IFO model

is inconsistent with situations when soot escapes to very lean mixtures unoxidized as in smoking flames. Soot could escape unoxidized either due to a suppressed oxidation rate or due to extremely fast transport. Even if not escaping unoxidized, soot may penetrate into leaner mixtures than Z_{soot} due to finite-rate oxidation. The transport of soot in Z-space is quantified using the mixture fraction displacement speed v_Z, defined as the relative motion between a diffusionless particle and a mixture fraction iso-surface, and expressed as [27]

$$v_Z = \frac{\nabla \cdot (\rho D \nabla Z)}{\rho |\nabla Z|}. \tag{28}$$

The velocity associated with this speed follows the opposite direction of the vector normal to the Z iso-surface. The D corresponds to the mixture fraction diffusivity with unity Lewis number.

To determine how far soot is transported in Z-space before being completely oxidized, the mixture fraction distance δ_Z is introduced and written as

$$\delta_Z = \frac{v_Z |\nabla Z|}{k_{\text{ox}}}. \tag{29}$$

Equation 29 measures the displacement of soot in Z-space in an interval of time equal to the characteristic time scale of oxidation (given by $1/k_{\text{ox}}$) and is evaluated at $Z = Z_{\text{soot}}$. A fast k_{ox} and slow v_Z will narrow δ_Z, so soot is oxidized rapidly, leading eventually to IFO. Conversely, a slow k_{ox} and fast v_Z will widen δ_Z, so soot oxidizes slowly and can penetrate further toward and potentially into fuel-lean mixtures. Since v_Z scales with the scalar dissipation rate, turbulent flames with high χ_{st} (or low local Damköhler number) could feature soot leakage into fuel-lean regions of the flame, which theoretically

could not be captured using IFO. Likewise, turbulent flames with locally suppressed oxidation (due either to heat losses or local extinction with high χ_{st}) could also feature soot leakage into fuel-lean regions of the flame, which also could not be captured using IFO.

The new presumed subfilter PDF for finite-rate oxidation of soot, hereafter referred as FRO, is related to a function depending also on Z and χ_{st}, with the following sooting mode $\widetilde{P}_S$:

$$\widetilde{P}_S = \delta\left(M_j - M_j^{\star}(Z, \chi_{st})\right), \tag{30}$$

where $M_j^{\star}(Z, \chi_{st}) = M_j^{\star\star}\mathcal{G}(Z, \chi_{\mathrm{st}})$ and $M_j^{\star\star}$ are chosen such that the convolution of $M_j^{\star}(Z, \chi_{st})$ against the joint subfilter PDF gives $\overline{M}_j$. Unlike the IFO model, the activation of the sooting mode is given with a smoother transition that begins just before Z_{soot}, which is described by a function $\mathcal{G}(Z, \chi_{\mathrm{st}})$ here proposed as

$$\mathcal{G}(Z, \chi_{\mathrm{st}}) = \frac{1}{2} + \frac{1}{2}\tanh\left(\frac{Z - (Z_{\mathrm{soot}} + \delta_Z/2)}{\delta_Z/2}\right). \tag{31}$$

Compared to the IFO model, the function $\mathcal{G}$ is continuous at Z_{soot} with a non-zero value. Like Z_{soot}, the mixture fraction distance δ_Z can be determined solely from information in mixture fraction space (so computed from the combustion model). This requires rewriting the displacement speed in mixture fraction space, which is given by

$$v_Z|\nabla Z| = \frac{1}{\rho}\nabla\cdot(\rho D\nabla Z) = \frac{1}{4\rho}\left[\frac{\chi}{D}\frac{\partial(\rho D)}{\partial Z} + \frac{\partial(\rho\chi)}{\partial Z}\right], \tag{32}$$

where the mixture fraction dissipation rate χ is analytically related to χ_{st} based on a presumed profile in mixture fraction space [28]. Only positive values of v_Z are considered in the model, and negative values (drifting toward

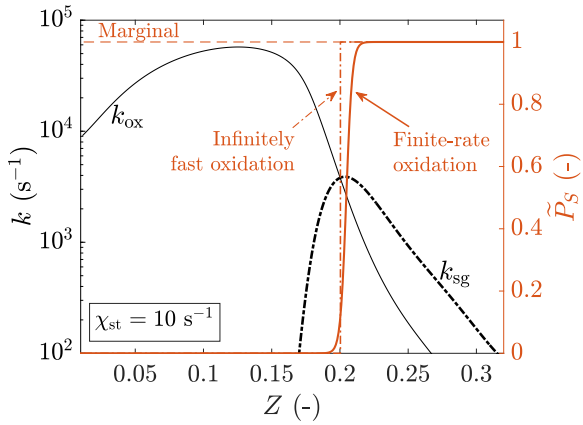

Figure 1: Sooting mode $\tilde{P}_S$ of the soot subfilter PDF models (Marg, IFO, and FRO) along with the rate coefficients of oxidation k_{ox} and surface growth k_{sg}, for a n-heptane non-premixed flame at $\chi_{\mathrm{st}} = 10\ \mathrm{s}^{-1}$ and similar conditions to the DNS presented in Section 4.

rich mixtures) are clipped to zero (*i.e.,* IFO). When the particles drift toward rich mixtures, they would not be oxidized, so this clipping has no influence on the ultimate results. Figure 1 shows an example of the sooting mode distribution $\tilde{P}_S$ in mixture fraction space using Marg, IFO, and FRO soot subfilter models in an n-heptane/air counterflow diffusion flame at $\chi_{\mathrm{st}} = 10\,\mathrm{s}^{-1}$ at similar conditions to the DNS presented in Section 4. The crossing of the oxidation and surface growth rates coefficients determine the mixture fraction crossing at $Z = Z_{\mathrm{soot}}$ and characterizes the activation of IFO and FRO models, where the latter is clearly admitting soot presence at leaner mixtures as indicated by the non-zero PDF value at mixture fractions less than Z_{soot}.

The filtered soot scalars can be expressed as a function of $M_j^{\star\star}$ as

$$\begin{aligned}\overline{M}_j &= \iint M_j P\left(M_j \mid \xi_k\right) \widetilde{P}\left(\xi_k\right) d\xi_k dM_j \\ &= (1-\omega) M_j^{\star\star} \int \mathcal{G}\left(Z, \chi_{\mathrm{st}}\right) \widetilde{P}\left(Z\right) dZ \\ &= \frac{\overline{M}_{0,0}^2}{\overline{M}_{0,0}^2} M_j^{\star\star},\end{aligned} \tag{33}$$

and, analogous to the IFO case, $M_j^{\star\star}$ can be rewritten as a function of the subfilter intermittency ω, the filtered soot scalars, and the integral of $\mathcal{G}(Z, \chi_{\mathrm{st}})$ against the thermochemical PDF $\widetilde{P}\left(Z\right)$, which is similar to what is obtained for IFO in Eq. 25:

$$M_j^{\star\star} = \frac{\overline{M}_j}{(1-\omega) \int \mathcal{G}(Z, \chi_{\mathrm{st}}) \widetilde{P}(Z) dZ}. \tag{34}$$

The subfilter intermittency with the FRO model is given by

$$\omega = 1 - \frac{1}{\int \mathcal{G}(Z, \chi_{\mathrm{st}}) \widetilde{P}(Z) dZ} \cdot \frac{\overline{M}_{0,0}^2}{\overline{M}_{0,0}^2}, \tag{35}$$

where the integral in the denominator can be calculated *a priori* for different χ_{st} as for the combustion model.

To determine the filtered source terms, the soot scalar source terms for oxidation (ox) and surface growth (sg) are written as in Eq. 20. Then, the filtered source terms for oxidation and surface growth are also obtained from

convolution against the joint subfilter PDF:

$$\begin{aligned}
\overline{\dot{M}_j}^{\mathrm{ox/sg}} &= \iint k_{\mathrm{ox/sg}}\left(\xi_k\right) f\left(M_j\right) P\left(M_j \mid \xi_k\right) \widetilde{P}\left(\xi_k\right) d\xi_k dM_j \\
&= \left[\int k_{\mathrm{ox/sg}}\left(\xi_k\right) \mathcal{G}\left(Z, \chi_{\mathrm{st}}\right) \widetilde{P}\left(\xi_k\right) d\xi_k\right] \left[(1-\omega) f\left(M_j^{\star\star}\right)\right] \\
&= \left[\frac{\int k_{\mathrm{ox/sg}}\left(\xi_k\right) \mathcal{G}\left(Z, \chi_{\mathrm{st}}\right) \widetilde{P}\left(\xi_k\right) d\xi_k}{\int \mathcal{G}\left(Z, \chi_{\mathrm{st}}\right) \widetilde{P}\left(\xi_k\right) d\xi_k}\right] \left[\frac{\overline{M}_{0,0}^2}{\overline{M}_{0,0}^2} f\left(M_j^{\star\star}\right)\right] \\
&= \hat{k}_{\mathrm{ox/sg}} \left[\frac{\overline{M}_{0,0}^2}{\overline{M}_{0,0}^2} f\left(M_j^{\star\star}\right)\right],
\end{aligned} \tag{36}$$

which is very similar to what is obtained for the marginal and IFO models in the previous subsection. Here, $\hat{k}_{\mathrm{ox/sg}}$ is the rate coefficient convoluted against the thermochemical PDF weighted by the $\mathcal{G}$-function of Eq. 31:

$$\hat{k}_{\mathrm{ox/sg}} = \left[\frac{\int k_{\mathrm{ox/sg}}\left(\xi_k\right) \mathcal{G}\left(Z, \chi_{\mathrm{st}}\right) \widetilde{P}\left(\xi_k\right) d\xi_k}{\int \mathcal{G}\left(Z, \chi_{\mathrm{st}}\right) \widetilde{P}\left(\xi_k\right) d\xi_k}\right]. \tag{37}$$

All quantities in Eq. 37 are functions of Z and χ_{st}, so $\hat{k}_{\mathrm{ox/sg}}$ can be pre-computed and stored in the thermochemical database, as was done for the marginal and IFO models [11] as stated in the previous subsection.

4. *A priori* validation against DNS data

In this Section, the new subfilter PDF model for finite-rate oxidation (FRO) of soot is assessed using a three-dimensional DNS database of turbulent nonpremixed temporally evolving planar jet flames at atmospheric pressure and two Damköhler numbers, from Attili *et al.* [13, 14]. *A priori* analyses are performed for the validation of the new model, including comparison to results from the previous Marg [4] and IFO [11] models.

4.1. DNS configuration

The DNS configurations consist of a nitrogen diluted n-heptane central stream (85% N_2 by volume) at 400 K and a coflowing stream of air at 800 K. The stoichiometric mixture fraction is $Z_{\rm st} = 0.147$. The initial velocity distribution in the fuel slab comes from an instantaneous realization of a turbulent channel flow at $\mathrm{Re}_\tau = 390$. Three cases were computed in Refs. [13, 14] by varying the Damköhler number and maintaining the jet Reynolds number $\mathrm{Re} = 2U_cH/\nu \approx 15000$, where U_c is the central jet velocity and H is the jet width. The initial thermochemical properties in all cases are the same. The velocities and lengths are rescaled to vary the Damköhler number. To evaluate the FRO model, only two cases are considered, corresponding to the medium and low Damköhler numbers ($\mathrm{Da}_M = 2\mathrm{Da}_L$).

The combustion kinetics of n-heptane consist of a reduced mechanism with 47 species and 290 reactions, that cover PAHs formation up to naphthalene [1]. Soot phenomena are modeled as in the previous section.

In the DNS, a discretized domain with $N_x \times N_y \times N_z = 1024 \times 1024 \times 512$ grid points was utilized. For additional information about the DNS configuration, the reader is referred to Ref. [14]. The strategy to analyze the DNS data is similar to Yang *et al.* [11], where a layer of $N_x \times N_y \times (\Delta/h + 1)$ points is extracted from the full grid, centered at $z_0/h = 256$, where Δ and h are respectively the filter and DNS grid spacing. This spanwise slice is located in the homogeneous mesh region where the element size is $h_M = 64.4$ μm and $h_L = 45.5$ μm for the Da_M and Da_L cases, respectively. The DNS data extracted for the analyses correspond to the same non-dimensional time $\tau = t/t_{jet}$ in both cases [14], where $t_{jet} = H/(2U_x)$ is the jet time scale,

corresponding to $t = 2.5$ ms and $t = 5$ ms for Da_L and Da_M, respectively.

LES model validation requires the application of a low-pass filter to the selected DNS snapshots. A three-dimensional, clipped and renormalized Gaussian filter kernel is utilized, following the work of Yang *et al.* [11]:

$$F\left(d_x, d_y, d_z\right) = \kappa^3 \exp\left[\frac{-6\left(d_x^2 + d_y^2 + d_z^2\right)}{\Delta^2}\right], \tag{38}$$

where Δ is the filter width, d_i are distances from a point of study in the Cartesian directions, and κ is a renormalization constant that guarantees the filter satisfies the following relationship:

$$\sum_{i=-\Delta/2h}^{\Delta/2h} \sum_{j=-\Delta/2h}^{\Delta/2h} \sum_{k=-\Delta/2h}^{\Delta/2h} F(ih, jh, kh) = 1, \tag{39}$$

where the filter kernel is active over a cube of $(\Delta/h + 1)^3$ grid points. This process is done by applying the Gaussian filter to groups of $(\Delta/h + 1)^3$ grid points.

4.2. Results: Oxidation and surface growth

The oxidation and surface growth filtered source terms, $\overline{\dot{M}}_{1,0}^{\mathrm{ox}}$ and $\overline{\dot{M}}_{1,0}^{\mathrm{sg}}$, are evaluated using the new FRO subfilter model, using Eq. 36, and compared against the Marg and IFO models. Building upon the strategy in the work of Yang *et al.* [11], rather than relying on a combustion model to obtain the oxidation and surface growth rate coefficients, these are obtained from the DNS database. In this work, these rate coefficients are obtained with a conditional average with respect to Z and χ_{st}:

$$k_{\mathrm{ox/sg}}(Z, \chi_{\mathrm{st}}) \approx \langle\ k_{\mathrm{ox/sg}}(x_j)\ \mid Z(x_j), \chi_{\mathrm{st}}(x_j)\rangle, \tag{40}$$

where $\langle \cdot \mid \xi_k \rangle$ symbolizes the density-weighted conditional averaging operator. It should be noted that Yang *et al.* [11] considered only single conditional averaging on Z. For the largest dissipation rates, Z_{soot} is undefined (*i.e.*, surface growth is never faster than oxidation), and, for these conditions, Z_{soot} then defaults to $Z_{\text{sg}}^{\max}$, that is, the mixture fraction corresponding to the maximum of the surface growth rate coefficient.

Soot oxidation and surface growth source terms depend on the total surface area moment $M_{0,1}$, which is included in the computations. Moreover, Yang *et al.* [11] showed that the subfilter β-PDF of mixture fraction $\widetilde{P}(Z)$ is sufficiently accurate to perform the analyses.

The filtered source terms for oxidation and surface growth using the Marg model [4] are written as

$$\overline{\dot{M}}_{1,0}^{\text{ox/sg}}(x_j) = \int_0^1 k_{\text{ox/sg}}(Z, \chi_{\text{st}}) \widetilde{P}(Z) dZ \cdot \overline{M}_{0,1}(x_j) \,. \tag{41}$$

From the equation above, the filtered source terms using the IFO model are

$$\overline{\dot{M}}_{1,0}^{\text{ox/sg}}(x_j) = \frac{\int_0^1 k_{\text{ox/sg}}(Z, \chi_{\text{st}}) H(Z, \chi_{\text{st}}) \widetilde{P}(Z) dZ}{\int_0^1 H(Z, \chi_{\text{st}}) \widetilde{P}(Z) dZ} \cdot \overline{M}_{0,1}(x_j), \tag{42}$$

where the convolution is "weighted" by the Heaviside function. Then, using the new FRO model the filtered source terms are calculated as:

$$\overline{\dot{M}}_{1,0}^{\text{ox/sg}}(x_j) = \frac{\int_0^1 k_{\text{ox/sg}}(Z, \chi_{\text{st}}) \mathcal{G}(Z, \chi_{\text{st}}) \widetilde{P}(Z) dZ}{\int_0^1 \mathcal{G}(Z, \chi_{\text{st}}) \widetilde{P}(Z) dZ} \cdot \overline{M}_{0,1}(x_j), \tag{43}$$

where the "weighting" is now carried out by the function $\mathcal{G}$ from Eq. 31.

In order to make a fair comparison against the DNS data, the filtered source terms of oxidation and surface growth are computed without using

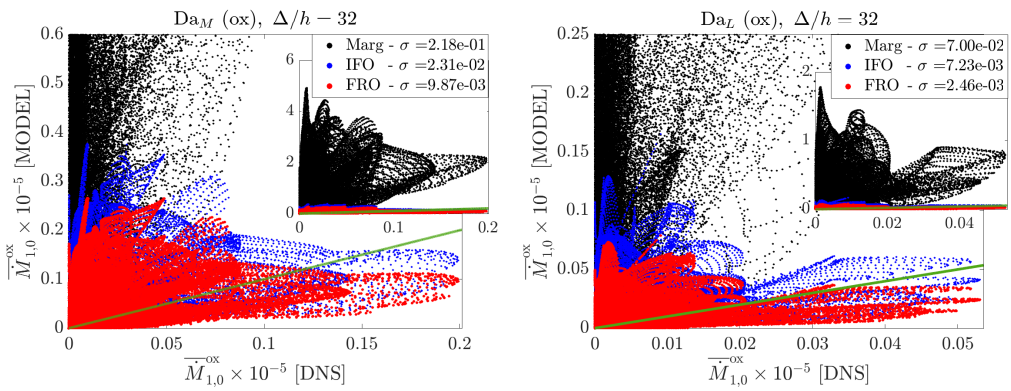

Figure 2: Comparison between the filtered DNS and the soot subfilter PDF models for the filtered oxidation source term. The standard deviation is indicated for each model.

any subfilter PDF but with the conditionally averaged rate coefficients:

$$\overline{\dot{M}}_{1,0}^{\rm ox/sg}(x_j) = \overline{k_{\rm ox/sg}\left(Z(x_j), \chi_{\rm st}(x_j)\right) \cdot M_{0,1}(x_j)}, \tag{44}$$

which is from now on referred as the filtered "DNS" case and $k_{\rm ox/sg}$ is the one from the model (Eq. 40).

Figure 2 shows parity plots of the filtered oxidation source terms $\overline{\dot{M}}_{1,0}^{\rm ox}$ at medium (left) and low (right) Damköhler numbers for the soot subfilter PDF models compared to the filtered DNS. The normalized filter width is $\Delta/h = 32$. Sample standard deviations σ are calculated and indicated in the plots. Marg is visibly overestimating the oxidation compared to the other models due to spurious oxidation [11], and the error σ is about 30 times greater than FRO (see zoomed out subfigure). Similar behavior was encountered in Ref. [11] compared to the IFO model. IFO and FRO seems to have a similar accuracy in the scatterplot, but, comparing the σ values, FRO is more than two times as accurate. Overall, the FRO model tends to reduce the slight overprediction of the magnitude of the oxidation source

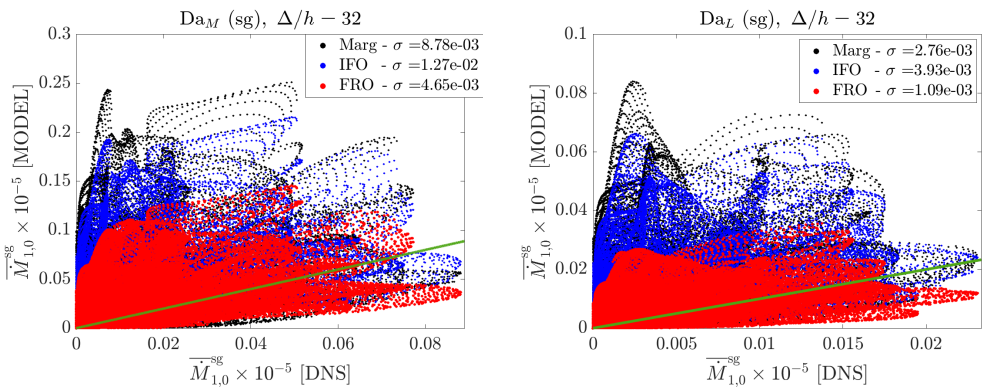

Figure 3: Comparison between the filtered DNS and the soot subfilter PDF models for the filtered surface growth source term. The standard deviation is indicated for each model.

term compared to the IFO model.

Likewise, Fig. 3 shows parity plots of the filtered surface growth source terms $\overline{\dot{M}}^{\mathrm{sg}}_{1,0}$ at medium (left) and low (right) Damköhler numbers for the soot subfilter PDF models compared to the filtered DNS. FRO is more accurate than IFO, with a σ of about three in Da_M and four in Da_L times smaller. It is interesting to note that the accuracy of the IFO model is actually worse than the Marg model, which contradicts the previous work of Yang *et al.* [11]. This difference is due to the double conditioning of the DNS data. Clearly, the Heaviside function in the IFO model can degrade the accuracy of the filtered surface growth source term. The FRO model, unlike the IFO model, improves prediction of oxidation compared to the Marg model without degrading predictions of surface growth. Indeed, as shown in Fig. 1, there is significant impact from an inclusion (respectively exclusion) of a portion of surface growth effects for mixtures with $Z < Z_{\mathrm{soot}}$ (respectively $Z > Z_{\mathrm{soot}}$) in the convolution operation of Eq. 37.

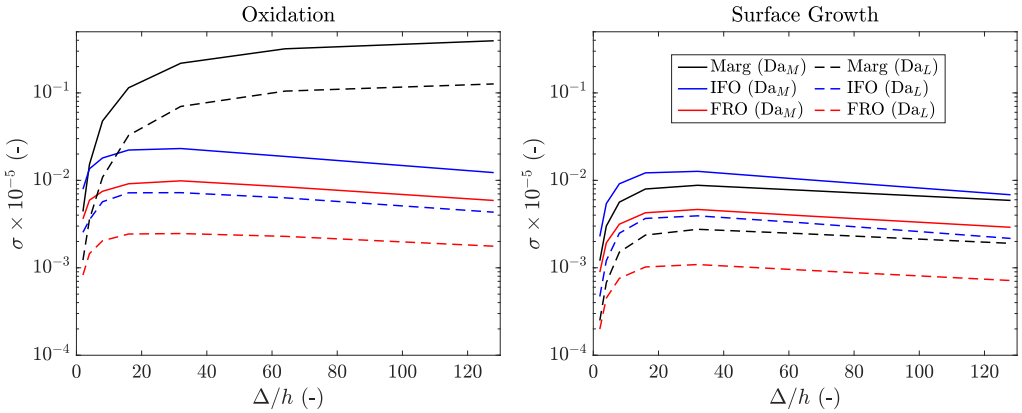

Figure 4: Influence of the relative filter width at medium (solid lines) and low (dashed lines) Damköhler number. Standard deviation σ of oxidation (left) and surface growth (right) source terms of the different soot subfilter PDF models against the DNS filtered data are compared.

4.3. Results: Influence of the filter width

The performance of the soot subfilter PDF models with varying the filter width for both Da_M and Da_L cases are shown in Fig. 4 along with the evolution of the error σ with the normalized filter width Δ/h ranging from 2 to 128 for the oxidation (left) and surface growth (right) filtered source terms.

In the medium Damköhler number case (continuous lines), predicting the filtered oxidation source term $\overline{\dot{M}}_{1,0}^{\mathrm{ox}}$ using Marg maintains a large error of up to two orders of magnitude compared to FRO. In general, FRO is much better than IFO and Marg as discussed in the previous subsection. For small relative filter widths ($\Delta/h < 8$), Marg decreases the discrepancies until it has similar performance to IFO and FRO. In other words, the subfilter model is paramount except for near-DNS resolution, where the accuracy becomes comparable.

For the low Damköhler number case (dashed lines in Fig. 4), the performances of the soot subfilter models on the oxidation source terms evolve with a similar fashion as in the medium Damköhler number case but with values lowered by a factor of 3 in average. Also, close to DNS resolution, IFO and Marg have the same accuracy and FRO double the performance. Regarding the surface growth filtered source term in Fig. 4 (right), the sample standard deviation σ evolution follows a similar trend as in the medium Da case. Moreover, similar to the oxidation case, the accuracy in all models is improved by a factor of 3 on average with the FRO model.

4.4. Analysis: Soot leakage at low Damköhler number

One of the motivations for developing the new subfilter model for finite-rate oxidation (FRO) is the ability to predict the existence of soot at leaner mixtures, which is theoretically disallowed in the IFO model. Attili *et al.* [14] found in their DNS data that soot leaks to fuel-lean mixtures in the low Damköhler number Da_L case at $t = 3.75$ ms, which was attributed to local weakening and flame quenching (so suppression of oxidation). In this subsection, an analysis is conducted to demonstrate the capability of the new FRO model in capturing soot leakage. The dataset for this analysis consists of a single plane from the DNS database, and only the FRO and IFO models are considered.

Figure 5 (left) shows a scatter plot of soot volume fraction f_v against the mixture fraction Z in black squares. The red circles indicate the points where $\mathcal{G}(Z, \chi_{\mathrm{st}}) > 0$ using the FRO model and relative filter size $\Delta/h = 4$. The blue triangles indicate the points where $H(Z, \chi_{\mathrm{st}}) > 0$ using the IFO model. The limits of $Z_{\mathrm{soot}}(\chi_{\mathrm{st}})$ are also indicated, $Z_{\mathrm{soot}}^{\mathrm{min}} = 0.18$ and $Z_{\mathrm{soot}}^{\mathrm{max}} = 0.3$ [11]. The

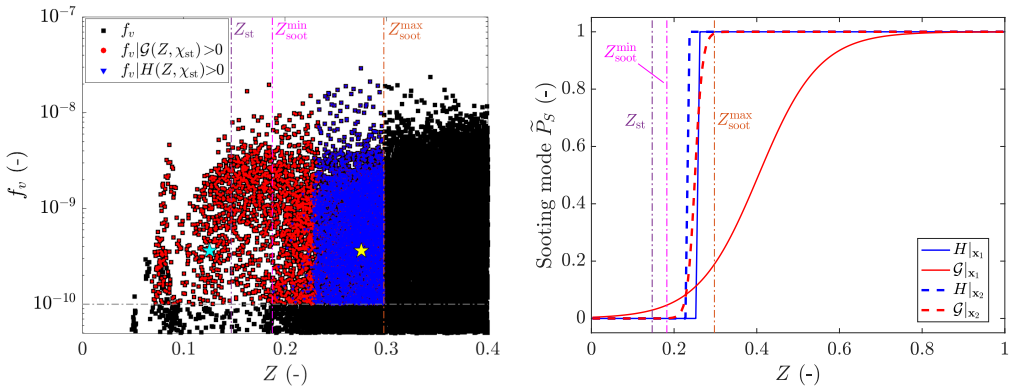

Figure 5: Left: Scatter of the soot volume fraction in the mixture fraction space in the Da_L case. Filtered data ($\Delta/h = 4$) using the FRO (red circles) and IFO (blue triangles) soot subfilter PDF models are also included. Vertical lines indicate the stoichiometric mixture fraction $Z_{\mathrm{st}} = 0.147$ and the limits of $Z_{\mathrm{soot}}(\chi_{\mathrm{st}})$: $Z_{\mathrm{soot}}^{\mathrm{min}} = 0.18$ and $Z_{\mathrm{soot}}^{\mathrm{max}} = 0.3$. The horizontal line indicates the minimum soot volume fraction considered in the analyses, which is consistent to Attili *et al.* [14]. Right: Sooting mode distributions $\widetilde{P}_S$ in the mixture fraction space for two points $\mathbf{x_1}$ (cyan star) and $\mathbf{x_2}$ (yellow star) extracted from the filtered data, using the IFO and FRO models, in the left subfigure.

FRO model can predict soot phenomena for $Z < Z_{\mathrm{soot}}^{\mathrm{min}}$, which correspond to about 9.3% of the events in $Z < Z_{\mathrm{soot}}^{\mathrm{max}}$. FRO can capture soot leakage across the flame front and even into fuel-lean regions ($Z \leq Z_{\mathrm{st}} = 0.147$), which represents the 5% of the events in $Z < Z_{\mathrm{soot}}^{\mathrm{max}}$. Only a few points with volume fractions greater than 0.1 ppb occur where $\mathcal{G} = 0$ and could not be captured by the FRO model, and these exclusively occur where the volume fraction is less than 0.3 ppb and for the leanest mixtures (*i.e.*, very likely representing soot that is just about finally burned out).

To characterize the sooting mode distributions in the lean and rich regions, two data points with the same soot volume fraction $f_v = 0.36$ ppb

are extracted and labeled as $\mathbf{x_1}$ (cyan star) and $\mathbf{x_2}$ (yellow star), shown in Fig. 5 (left), where $\xi(\mathbf{x_1}) = \{Z = 0.125,\ \chi_{\rm st} = 500\,{\rm s}^{-1}\}$ and $\xi(\mathbf{x_2}) = \{Z = 0.275,\ \chi_{\rm st} = 100\,{\rm s}^{-1}\}$. The plot of Fig. 5 (right) shows the sooting mode distributions $H(Z, \chi_{\rm st})$ (IFO) and $\mathcal{G}(Z, \chi_{\rm st})$ (FRO). At $\mathbf{x_1}$, the FRO model shows a wide transition in the sooting mode and correctly allows for some soot at this very lean mixture. Conversely, using the IFO, the sharp transition at $Z_{\rm soot}$ does not capture the leakage effects to lean mixture fractions. At $\mathbf{x_2}$, the FRO model exhibits a much narrower width in mixture fraction space and is almost the same as the IFO model since the soot at this rich mixture fraction will not penetrate to leaner mixtures. Therefore, as demonstrated, the FRO model, unlike the IFO model, is capable of correctly predicting the leakage of soot to leaner mixture fractions, consistent with the DNS data of Attili *et al.* [14].

To assess the potential of the new soot subfilter model in the soot leakage region, the filtered soot oxidation source terms $\overline{\dot{M}}_{1,0}^{\rm ox}$ are compared between the FRO and IFO models. The analysis is made in the fuel-lean part of the soot leakage region where $Z < 0.1$ and soot volume fraction $f_v \geq 0.1$ ppb, in order to be at the same range as in Ref. [14], and restricted to points where the thermochemical PDF (beta distribution) is greater than 1% over this mixture fraction range. Parity plots are shown in Fig. 6, using different relative filter widths $\Delta/h = 2$, 4, 8, and 16. The discrepancies of the models against the DNS are quantified using the standard deviation σ as in previous subsections and are indicated in the upper-left corner of each subfigure. The prediction of the oxidation source terms using the FRO model agrees very well with the filtered DNS data. As the size of the relative filter width

increases, the FRO model performance decreases slightly but is still superior to the IFO. At $\Delta/h = 16$, the FRO model declines in performance and later, at $\Delta/h = 32$ and on, it degenerates into a similar shape and error value as IFO (not shown). Additionally, it should be noted that a few points with the FRO model incorrectly predict zero source term, which occurs due to an underprediction of the width of the FRO model in mixture fraction space. The soot particles are driven to the fuel-lean regions by transport effects induced by the locally fast strain rates. As a final note, since the Heaviside function of IFO is zero in this fuel-lean region so no soot present, the filtered oxidation source includes contributions only from richer mixtures where the beta distribution of mixture fraction is non-zero.

5. *A posteriori* validation: LES of the Sandia flame

In this section, additional *a posteriori* LES evaluation of the soot subfilter PDF models is conducted. The flame configuration selected is the Sandia turbulent nonpremixed jet flame, introduced by Zhang *et al.* [17]. LES results obtained with the three subfilter PDF models are compared with experimental measurements.

5.1. Experimental setup

The Sandia flame from Ref. [17] consists of a turbulent nonpremixed piloted jet flame at atmospheric pressure. Pure ethylene is injected at the central jet with $\mathrm{Re} = 20,000$, where the bulk velocity is 54.7 m/s and the jet inner diameter is $D = 3.2$ mm. The pilot flame, with outer diameter of 19.1 mm, is obtained from an ethylene-air premixture at $\phi = 0.9$, in order to acquire a thermal power equivalent to 2% of the main jet. A surrounding air

coflow is injected at 0.6 m/s to isolate the flame from external perturbations. More characteristics about the burner can be found in Zhang *et al.* [17]. The experimental database used for the comparisons in this work includes mean and RMS temperature profiles [29], mean and RMS soot volume fraction profiles [30, 31], resolved soot intermittency and soot temperature profiles [30], and chemical species profiles such as OH [17, 30].

5.2. Computational framework

Computational simulations are carried out in NGA, a finite difference code for grid-filtered LES of low-Mach number turbulent reacting flows [32, 33]. The computational domain of the Sandia burner consists of a structured cylindrical mesh of $192 \times 96 \times 32$ points in the streamwise, radial, and circumferential directions, respectively. The dimensions of the domain are $300D \times 70D$ in the streamwise and radial direction, respectively. The grid is taken from Yang *et al.* [11], which stretches the cells in both radial and streamwise directions. The central jet unsteady velocity inflow profile was generated using a simulation of flow through a periodic pipe.

The thermochemical database consists of solutions to the nonpremixed flamelet equations with radiative heat losses (RFPV) computed with FlameMaster [34]. As discussed in subsection 2.2, the RFPV database is parameterized by $\widetilde{Z}$, Z_v, $\widetilde{C}$, and $\widetilde{H}$ with a resolution of 100 divisions per parameter. The combustion chemistry (158 species and 1804 reactions.) used to generate the RFPV database is from Blanquart *et al.* [35], which covers gas-phase kinetics for ethylene up to 4-rings PAHs ($C_{18}H_{10}$), and Narayanaswamy *et al.* [36], which extends the previous kinetics to account for high-temperature oxidation of substituted aromatic species.

5.3. Results: Temperature and soot volume fraction

Figure 7 shows the radial profiles of mean (top) and RMS (bottom) temperature at two different locations downstream the burner exit: $x/D = 134$ (left) and $x/D = 175$ (right). A comparison is made between computational results using the Marg, IFO, and FRO soot subfilter models and experimental measurements [29].

At both positions, the mean temperature predicted by Marg is higher than the other models and the experimental measurements, which is accentuated at $x/D = 175$ with about 300 K of disagreement at the centerline. This is because the Marg model underpredicts soot, as shown below, so soot radiation [11]. However, using IFO and FRO, the computational results compare favorably with the experimental measurements, albeit with a slight underprediction.

The RMS temperature plots in Fig. 7 (bottom) show more significant differences between computational results and experimental measurements at both axial positions. The computational results only include the resolved contribution to the RMS, and, on this coarse grid, the unresolved subfilter temperature variance is not an insignificant contribution. However, the results indicate good agreement with the experimental measurements nonetheless.

To better see the influence of the soot subfilter model on the temperature evolution, the temperature profile along the centerline is shown in Fig. 8. Results show that the Marg model overpredicts the temperature for $x/D > 100$ with a maximum difference of about 700 K at $x/D \approx 240$. The lack of soot using the Marg model (see Fig. 10) makes it unable to predict the

correct amount of radiative losses in the flame. However, IFO and FRO show almost identical temperature profiles and agree well with the experimental data, which suggest the amount of soot produced in both models is about the same.

Mean (top) and normalized RMS (bottom) soot volume fraction profiles are plotted in Fig. 9 at different axial positions: $x/D = 70.3$, $x/D = 132.8$, and $x/D = 195.3$. Computational results using the three soot subfilter PDF models and experimental measurements [31] are compared.

Mean profiles show that FRO model captures better the soot volume fraction f_v in the upstream portion of the sooting region of the flame ($x/D = 70.3$). Then, at about the middle of the sooting region ($x/D = 132.8$), the IFO and FRO models overpredict experimental measurements at the centerline by about a factor of three. Further downstream at $x/D = 195.3$, soot is overpredicted by a factor of two using the IFO and FRO models. In all cases the Marg model overpredicts oxidation, so the mean f_v is almost zero in the entire flame, as discussed by Yang *et al.* [11]. A more detailed analysis at $x/D = 70.3$, in Fig. 9 (left), where FRO indicates a significant improvement over IFO, will be presented in a later section.

The soot volume fraction fluctuations are scaled by the mean since the mean values shown above differ with the experiments. The normalized RMS profiles of soot volume fraction, obtained by dividing the RMS values by the mean values, are plotted in Fig. 9 (bottom) and show that soot fluctuations levels are better captured using the FRO and IFO models (except for the IFO model in the upstream region). In general, these two models capture very well the fluctuations in the sooting region ($r/D \leq 10$) and beyond that,

since soot predicted is negligible, the relative fluctuations grow abruptly. Since the Marg model incorrectly predicts the mean soot volume fraction, the fluctuations are quite inaccurate, being extremely underpredicted in the far upstream region to overpredicted in the downstream region.

The mean soot volume fraction profile along the centerline is plotted in Fig. 10 and compares the computational results obtained with the three soot subfilter models and experimental measurements [17]. The Marg model underpredicts the maximum soot volume fraction value by a factor of more than 20 compared to experimental measurements. The IFO and FRO model predict the same maximum value of soot volume fraction and the peak position slightly shifted downstream the burner by a distance of about $15D$ compared to the experimental measurements. However, the new FRO subfilter model can capture better the inception zone starting at $x/D = 40$ through $x/D = 80$, where relatively high strain rate has been observed in experiments [30]. This is consistent with the *a priori* analysis of Section 4 at the low Damköhler number case, in which better performance of the FRO model is obtained. Moving downstream, χ_{st} decreases, and the regime becomes more similar to the medium Damköhler number case, where soot surface growth is less accurate and therefore overpredicted with the IFO model. Since the IFO model overpredicts the surface growth more than FRO, the mean soot volume fraction with IFO increases much more rapidly even though reaching the same maximum value (due to a comparable overprediction of both surface growth and oxidation). Further downstream, IFO overestimates oxidation compared to FRO, so f_v decreases more rapidly ($x/D = 200$) and FRO predicts soot for a longer extent consistent with the experimental measurements.

Overall, since the IFO model overpredicts both surface growth and oxidation, the increase and decrease of soot is faster than the FRO model (and the experimental measurements), and soot is confined to a streamwise region that is more compact than the FRO model (and the experimental measurements) even though reaching the same maximum soot volume fraction.

5.4. Results: Soot intermittency and soot temperature

The resolved soot intermittency in the Sandia flame was studied experimentally by Shaddix *et al.* [30] and indicates the probability of not encountering soot in space and time contingent on a threshold value of soot volume fraction experimentally established. This value was set to $f_v = 0.03$ ppm [30]. A probability of one indicates that no soot was detected over the experimental threshold. To further validate the soot subfilter models and understand the discrepancies in the previous section, computational results using IFO and FRO soot subfilter models are compared against experimental measurements from Ref. [30].

Figure 11 shows the resolved intermittency profile along the centerline. The computational results indicate a correspondence to the mean soot volume fraction profile in Fig. 10, where the FRO model is in better agreement than IFO to experimental results at the beginning and at the end of the sooting region. Both models overestimate the soot presence in the growth region, but this is not unexpected with the overprediction of the mean soot volume fraction. Briefly, the LES results predict more and consistent soot so are overpredicting the mean soot volume fraction but underpredicting the intermittency and normalized RMS near the maximum of the mean soot volume fraction compared to the experimental measurements. The source

of this more consistent and less intermittent nature of soot predicted by the LES model requires further investigation.

Experimental measurements of the soot temperature are also available [17]. This is determined by averaging the temperature where soot is present (*i.e., when the resolved intermittency is zero)* in the turbulent flame and is linked to the location of soot in the mixture fraction space. Figure 12 illustrates the centerline profiles of the soot temperature T_{soot} using IFO and FRO subfilter models and the experimental data. T_{soot} is well predicted by both models between $x/D = 75$ and $x/D = 200$. In the upstream and downstream portions of the sooting region, the soot temperature is underpredicted by FRO (no soot present in IFO model). The explanation for this discrepancy could be attributed to two possible effects. In the upstream region, this could indicate that soot forms at mixture fractions richer than the experimental measurements, and, in the downstream region, this could indicate excessive soot radiation. However, there are no experimental measurements to confirm these possibilities.

5.5. Results: Soot source terms

The variation of soot volume fraction predictions obtained in Fig. 10 could be attributed to the effects of the soot subfilter PDF models on the mixing and flow field, or on the soot source terms [11]. Therefore, both causes will be examined in the Sandia flame.

Figure 13 shows the mean mixture fraction along the centerline using the three soot subfilter models. All of the subfilter models predict similar values of Z, so all models have no effect on the mixing and flow field. Similar conclusions were obtained for a different flame by Yang *et al.* [11]. Therefore,

the differences between results obtained with different soot subfilter PDF models come from the impact of the soot subfilter PDF models on the soot source terms.

In the *a priori* analysis, the soot subfilter models were shown to fundamentally exert influence on the oxidation and surface growth source terms. To analyze these source terms from the LES results, the source terms are normalized because they depend on the predicted amount soot. As observed in Figs. 10 and 11, the new FRO model is superior to the IFO model at the beginning and at the end of the sooting region, and the analysis will be focused on those regions. Figure 14 show the conditional normalized source terms of oxidation (top) and surface growth (bottom) in mixture fraction at two axial positions $x/D = 100$ and $x/D = 205$. The interval of Z is selected such that the conditional soot volume fraction is greater than zero.

The normalized oxidation source term using the Marg model is greater than the other two models in both locations, with differences up to two orders of magnitude. These results agrees to what it was observed in the *a priori* analysis in Section 4. The gap between the IFO and FRO models is smaller. At $x/D = 100$, the maximum difference takes place at $Z = 0.11$ where IFO predicts a source term with double the value obtained using FRO. At $x/D = 205$ this difference is reduced, with a 40% difference near the stoichiometric value of mixture fraction ($Z_{\mathrm{st}} = 0.0635$).

The normalized surface growth source terms in Fig. 14 (bottom) exhibits a different trend, where in general they are at the same order of magnitude. Similar to the oxidation case, the Marg model overestimates surface growth at both axial positions compared to FRO, with maximum differences of a

factor of about three at $x/D = 100$ and up to eight at $x/D = 205$. However, since oxidation is extremely overpredicted, soot cannot grow using the Marg model. The difference between IFO and FRO are in the same proportion as in the oxidation case. At $x/D = 100$, the ratio between IFO and FRO predictions at $Z = 0.11$ is about 1.75, and at $x/D = 205$ the ratio near the stoichiometric mixture is about two.

Nonetheless, these results verify the discussion at the end of subsection 5.3. At $x/D = 100$, the more dominant surface growth term is larger for IFO compared to FRO, which results in sharper growth around this location (see Fig. 10). Conversely, at $x/D = 205$, the dominant oxidation term is larger for IFO than FRO, which results in a more rapid decrease of soot (see Figs. 10 and 11). As shown in Fig. 5, compared to the experimental measurements, the qualitative behavior of the FRO model is correct.

5.6. Further analysis: Soot leakage in the Sandia flame

As discussed before, at high χ_{st} or low local Damköhler numbers soot might overcome oxidation and escape to fuel-lean regions. In the Sandia flame, Shaddix *et al.* [30] experimentally observed soot leakage by superimposing OH PLIF imaging with LII soot observations, at a distance relatively close to the burner exit ($x/D \approx 70$) where the flow still exhibits high strain rate (high χ_{st}) but soot starts to grow. The measurements indicated sometimes an overlap of soot from the LII image with (weak) OH from the PLIF image. In order to further validate the new soot subfilter model and confirm what discussed in subsection 4.4, a further comparison of computational results of soot and OH using the IFO and FRO soot subfilter PDF models against experimental measurements is conducted.

Rather than qualitative comparisons of two images, the presence of soot leakage in the computational results is assessed through conditional statistics. Figure 15 (left) illustrates the conditional soot volume fraction $\langle f_v \mid Z \rangle$ at the axial position $x/D = 70.3$ in mixture fraction and shows that soot leakage is indeed predicted by the new FRO model (vertical line indicates the stoichiometric mixture Z_{st}), while the conditional volume fraction predicted by the IFO model is negligibly small for fuel-lean mixtures (*i.e.*, no leakage). The conditional OH mass fraction $\langle Y_{\mathrm{OH}} \mid Z \rangle$ is also included and confirms that soot leakage is occurring into regions where OH is (at least sometimes) present.

Figure 15 (right) shows the radial profiles of soot volume fraction (extracted from Fig. 9) and normalized OH mass fraction at $x/D = 70.3$. For the latter, the normalized OH presence is obtained computationally by dividing the mean OH mass fraction profile by its maximum value $Y_{\mathrm{OH}}/Y_{\mathrm{OH}}^{\mathrm{max}}$ and experimentally by dividing the OH PLIF signal [17, 30] by its maximum value $[\mathrm{OH} \cdot \mathrm{PLIF}]/[\mathrm{OH} \cdot \mathrm{PLIF}]^{\mathrm{max}}$. The vertical line indicates the spatial position of the mean stoichiometric mixture fraction. With the FRO model, both profiles are quantitatively consistent with the experimental measurements (albeit soot slightly overpredicted).

These results validate the capability of the FRO model to capture soot leakage into fuel-lean regions. However, further studies are needed in turbulent smoking flames to extensively validate the new soot subfilter model, which is left for future work.

6. Conclusions

In this work, a new presumed filter PDF model is proposed to capture finite-rate oxidation (FRO) of soot particles in turbulent reacting flows. This new model corrects the inconsistencies of previous models. The model not only eliminates spurious oxidation but also allow for the capturing of soot leakage into fuel-lean mixtures either when the oxidation rate is slow or when the turbulent transport is fast, for instance, in turbulent smoking flames.

A priori analyses and validation of the FRO model have been conducted using DNS data of turbulent nonpremixed flames with medium (Da_M) and low (Da_L) Damköhler numbers. Results indicate a significant improvement in the prediction of oxidation source term compared to previous models, which achieve an accuracy increase of two (respectively three) times to an order of magnitude in the Da_M (respectively Da_L) case. Overall, results indicate that the new FRO model improves oxidation predictions without degrading the predictions of surface growth as opposed to previous models. Finally, the potential to capture soot leakage using the FRO model was assessed, showing very good agreement with the filtered DNS data.

A substantial *a posteriori* validation was carried out in a turbulent nonpremixed sooting jet flame. The new soot subfilter PDF model was implemented within an LES framework and results where compared to previous models, the Marginal (Marg) and Infinitely Fast Oxidation (IFO) models, and experimental measurements. Temperature results using the FRO model show similar agreement compared with the IFO model, while the Marg model tends to overpredict it because of the incorrect prediction of soot so underprediction of radiative heat losses. Computational results of soot volume

fraction show an extreme underprediction using the Marg model compared to experiments, while good predictions are found using FRO and IFO. The FRO model however is able to capture better the initial and final stages of the sooting region across the flame. The soot source terms of oxidation and surface growth were later studied at the initial and final portion of the sooting region, which explains the mechanism of soot evolution using the three models and also why previous models overpredict oxidation or surface growth, confirming what was observed in the soot volume fraction discussion. Finally, to consolidate the capability of the FRO model to capture the soot leakage in fuel-lean regions, an analysis of the computational results using FRO and IFO models shows that the FRO model indeed agrees with experimental measurements (while IFO fails), where the sooting region begins and the strain rate is still relatively high, and confirms the observations of the *a priori* analyses. Nevertheless, additional investigation might be needed to extensively validate the new FRO model in other situations, for instance, in turbulent smoking flames (such as the JP-8 Sandia flame [17], where much more soot leakage was experimentally observed) and turbulent pressurized flames, which will be addressed in the future.

Acknowledgments

The authors gratefully acknowledge funding from NASA under grant NNX16AP90A and NSF under grant CBET-2028318. The authors also acknowledge valuable support in the form of computational time on the Tiger high performance computer center at Princeton University, which is jointly supported by the Princeton Institute for Computational Science and Engi-

neering (PICSciE) and the Princeton University Office of Information Technology's Research Computing department.

References

[1] F. Bisetti, G. Blanquart, M. E. Mueller, H. Pitsch, On the formation and early evolution of soot in turbulent nonpremixed flames, Combustion and Flame 159 (2012) 317–335.

[2] B. Franzelli, P. Scouflaire, S. Candel, Time-resolved spatial patterns and interactions of soot, pah and oh in a turbulent diffusion flame, Proceedings of the Combustion Institute 35 (2015) 1921–1929.

[3] F. Bisetti, A. Attili, H. Pitsch, Advancing predictive models for particulate formation in turbulent flames via massively parallel direct numerical simulations, Philosophical Transactions of the Royal Society A: Mathematical, Physical and Engineering Sciences 372 (2014) 20130324.

[4] M. E. Mueller, H. Pitsch, Large eddy simulation subfilter modeling of soot-turbulence interactions, Phys. Fluids 23 (2011) 115104.

[5] A. Wick, F. Priesack, H. Pitsch, Large-eddy simulation and detailed modeling of soot evolution in a model aero engine combustor, in: Turbo Expo: Power for Land, Sea, and Air, volume 50848, American Society of Mechanical Engineers, 2017, p. V04AT04A020.

[6] H. Koo, M. Hassanaly, V. Raman, M. E. Mueller, K. Peter Geigle, Large-eddy simulation of soot formation in a model gas turbine combustor, Journal of Engineering for Gas Turbines and Power 139 (2017).

[7] S. T. Chong, V. Raman, M. E. Mueller, P. Selvaraj, H. G. Im, Effect of soot model, moment method, and chemical kinetics on soot formation in a model aircraft combustor, Proceedings of the Combustion Institute 37 (2019) 1065–1074.

[8] P. Rodrigues, B. Franzelli, R. Vicquelin, O. Gicquel, N. Darabiha, Coupling an LES approach and a soot sectional model for the study of sooting turbulent non-premixed flames, Combustion and Flame 190 (2018) 477–499.

[9] B. Franzelli, A. Vié, N. Darabiha, A three-equation model for the prediction of soot emissions in les of gas turbines, Proceedings of the Combustion Institute 37 (2019) 5411–5419.

[10] L. Berger, A. Wick, A. Attili, M. E. Mueller, H. Pitsch, Modeling subfilter soot-turbulence interactions in Large Eddy Simulation: An a priori study, Proc. Combust. Inst. 38 (2021) 2783–2790.

[11] S. Yang, J. K. Lew, M. E. Mueller, Large Eddy Simulation of soot evolution in turbulent reacting flows: Presumed subfilter PDF model for soot–turbulence–chemistry interactions, Combust. Flame 209 (2019) 200–213.

[12] J. Kent, S. Bastin, Parametric effects on sooting in turbulent acetylene diffusion flames, Combust. Flame 56 (1984) 29–42.

[13] A. Attili, F. Bisetti, M. E. Mueller, H. Pitsch, Formation, growth, and transport of soot in a three-dimensional turbulent non-premixed jet flame, Combust. Flame 161 (2014) 1849–1865.

[14] A. Attili, F. Bisetti, M. E. Mueller, H. Pitsch, Damköhler number effects on soot formation and growth in turbulent nonpremixed flames, Proc. Combust. Inst. 35 (2015) 1215–1223.

[15] M. E. Mueller, G. Blanquart, H. Pitsch, Hybrid method of moments for modeling soot formation and growth, Combust. Flame 156 (2009) 1143–1155.

[16] M. E. Mueller, H. Pitsch, LES model for sooting turbulent nonpremixed flames, Combust. Flame 159 (2012) 2166–2180.

[17] J. Zhang, C. R. Shaddix, R. W. Schefer, Design of "model-friendly" turbulent non-premixed jet burners for C2+ hydrocarbon fuels, Rev. Sci. Inst. 82 (2011) 074101.

[18] M. E. Mueller, G. Blanquart, H. Pitsch, A joint volume-surface model of soot aggregation with the method of moments, Proc. Combust. Inst. 32 (2009) 785–792.

[19] M. E. Mueller, G. Blanquart, H. Pitsch, Modeling the oxidation-induced fragmentation of soot aggregates in laminar flames, Proc. Combust. Inst. 33 (2011) 667–674.

[20] M. Ihme, H. Pitsch, Modeling of radiation and nitric oxide formation in turbulent nonpremixed flames using a flamelet/progress variable formulation, Phys. Fluids 20 (2008) 055110.

[21] R. Barlow, A. Karpetis, J. Frank, J.-Y. Chen, Scalar profiles and no formation in laminar opposed-flow partially premixed methane/air flames, Combust. Flame 127 (2001) 2102–2118.

[22] G. Hubbard, C. Tien, Infrared mean absorption coefficients of luminous flames and smoke, J. Heat. Transf. 100 (1978) 287–305.

[23] M. E. Mueller, Physically-derived reduced-order manifold-based modeling for multi-modal turbulent combustion, Combust. Flame 214 (2020) 287–305.

[24] A. Attili, F. Bisetti, M. E. Mueller, H. Pitsch, Effects of non-unity lewis number of gas-phase species in turbulent nonpremixed sooting flames, Combust. Flame 166 (2016) 192–202.

[25] S. Yang, J. K. Lew, M. E. Mueller, Large Eddy Simulation of soot evolution in turbulent reacting flows: Strain-sensitive transport approach for polycyclic aromatic hydrocarbons, Combust. Flame 220 (2020) 219–234.

[26] A. W. Cook, J. J. Riley, A subgrid model for equilibrium chemistry in turbulent flows, Phys. fluids 6 (1994) 2868–2870.

[27] S. Pope, The evolution of surfaces in turbulence, Int. J. Eng. Sci. 26 (1988) 445–469.

[28] N. Peters, Local quenching due to flame stretch and non-premixed turbulent combustion, Combust. Sci. Technol. 30 (1983) 1–17.

[29] S. P. Kearney, D. R. Guildenbecher, C. Winters, P. A. Farias, T. W. Grasser, J. C. Hewson, Temperature, Oxygen, and Soot-Volume-Fraction Measurements in a Turbulent C2H4-Fueled Jet Flame, Technical Report SAND2015-7968, Sandia National Lab.(SNL-NM), Albuquerque, NM (United States), 2015.

[30] C. R. Shaddix, J. Zhang, R. W. Schefer, J. Doom, J. C. Oefelein, S. Kook, L. M. Pickett, H. Wang, Understanding and predicting soot generation in turbulent non-premixed jet flames, Sand2010-7178, Sandia Report (2010).

[31] C. R. Shaddix, J. Zhang, T. Williams, Quantifying soot concentrations in turbulent non-premixed jet flames., in: Spring Meeting Western States Section of the Combustion Institute, 2016.

[32] O. Desjardins, G. Blanquart, G. Balarac, H. Pitsch, High order conservative finite difference scheme for variable density low mach number turbulent flows, J. Comput. Phys. 227 (2008) 7125–7159.

[33] J. F. MacArt, M. E. Mueller, Semi-implicit iterative methods for low mach number turbulent reacting flows: Operator splitting versus approximate factorization, J. Comput. Phys. 326 (2016) 569–595.

[34] H. Pitsch, Flamemaster: A C++ computer program for 0d combustion and 1d laminar flame calculations, URL: http://www. itv. rwth-aachen. de/en/downloads/flamemaster 81 (1998).

[35] G. Blanquart, P. Pepiot-Desjardins, H. Pitsch, Chemical mechanism for high temperature combustion of engine relevant fuels with emphasis on soot precursors, Combust. Flame 156 (2009) 588–607.

[36] K. Narayanaswamy, G. Blanquart, H. Pitsch, A consistent chemical mechanism for oxidation of substituted aromatic species, Combust. Flame 157 (2010) 1879–1898.

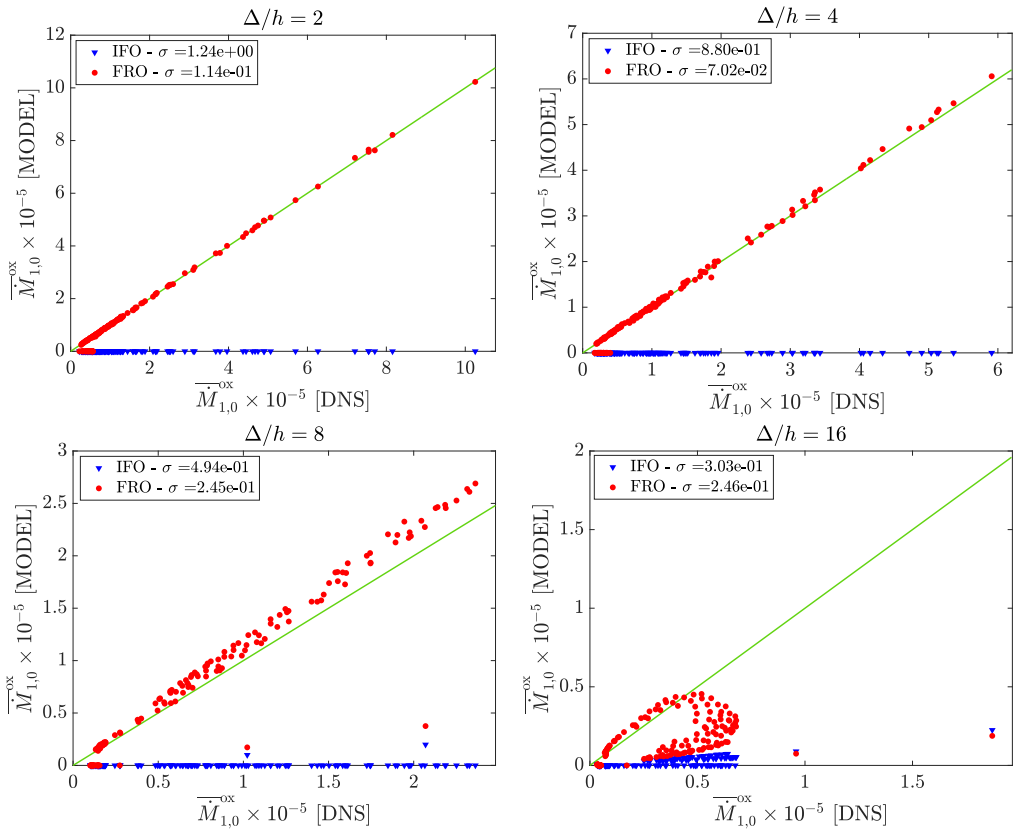

Figure 6: Parity plots of filtered soot oxidation source term using IFO and FRO soot subfilter models versus the DNS filtered case. The analyzed data correspond to grid points belonging to the lean soot leakage region ($Z < 0.1$) and using different relative filter width Δ/h. The standard deviation is indicated for each model.

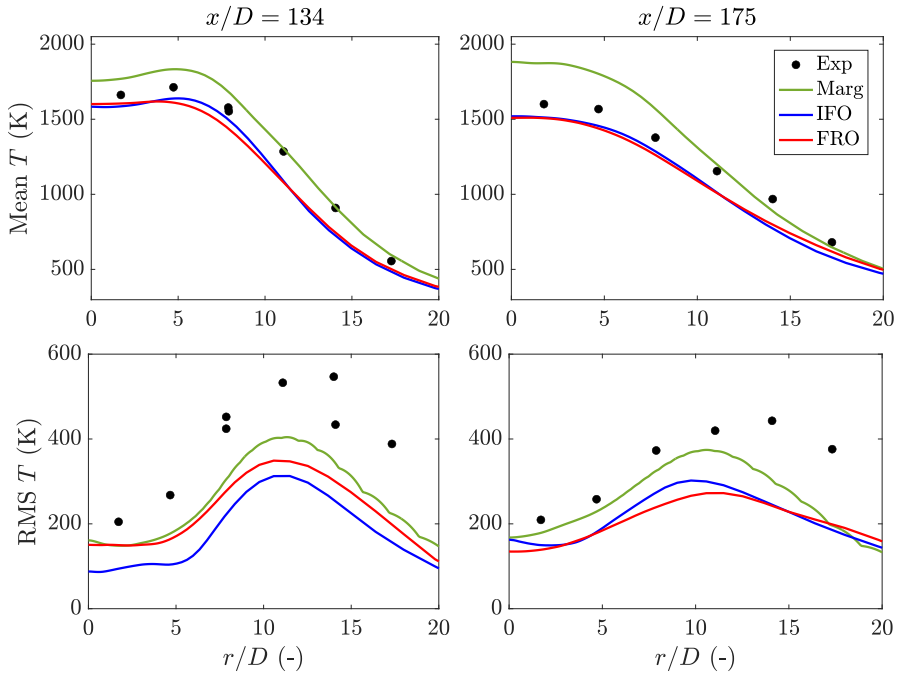

Figure 7: Mean (top) and RMS (bottom) temperature radial profiles at two different positions above the Sandia burner: $x/D = 134$ (left) and $x/D = 175$ (right). Comparison of computational results using the three soot subfilter models and experimental measurements from Ref. [29].

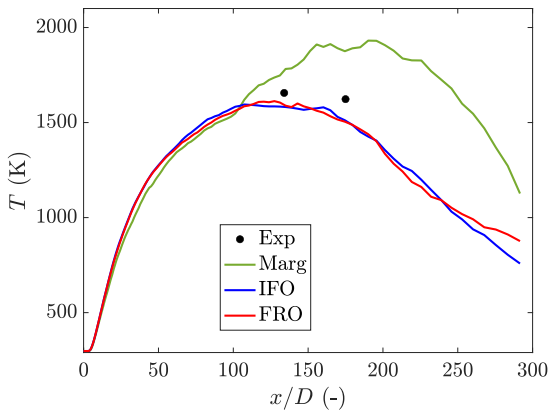

Figure 8: Mean temperature profiles along the centerline in the Sandia burner. Comparison of computational results using the three soot subfilter PDF models and two experimental points from Ref. [29].

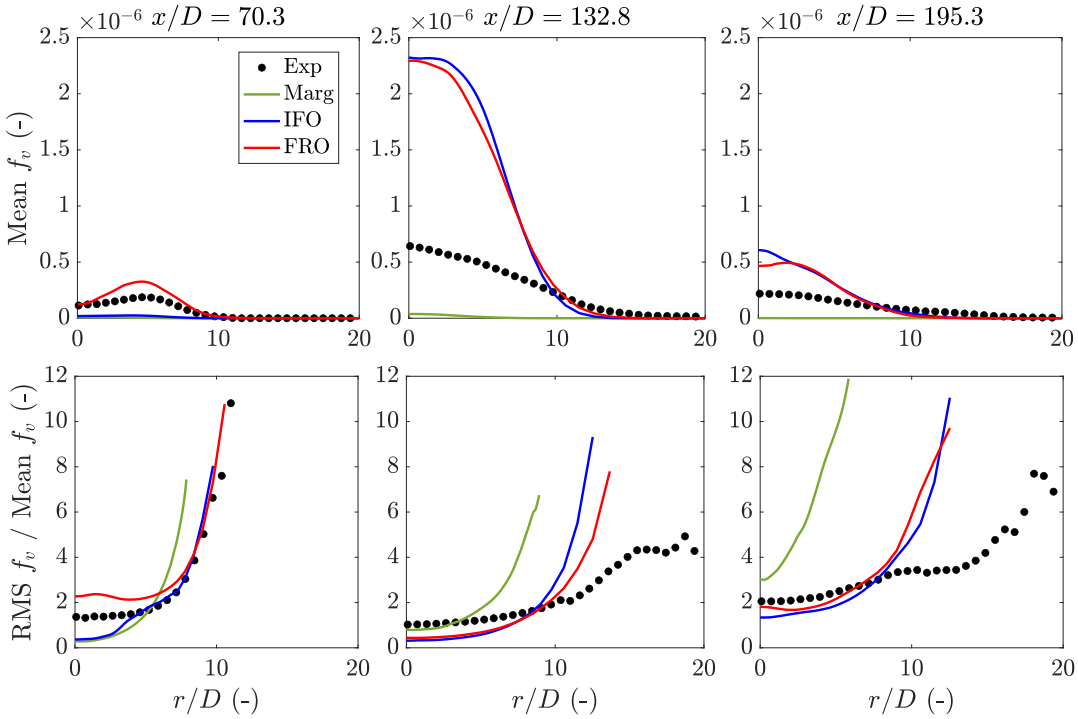

Figure 9: Mean (top) and normalized RMS (bottom) soot volume fraction radial profiles at three different positions above the Sandia burner: $x/D = 70.3$ (left), $x/D = 132.8$ (middle) and $x/D = 195.3$ (right). Comparison of computational results using the three soot subfilter PDF models and experimental measurements from Ref. [31].

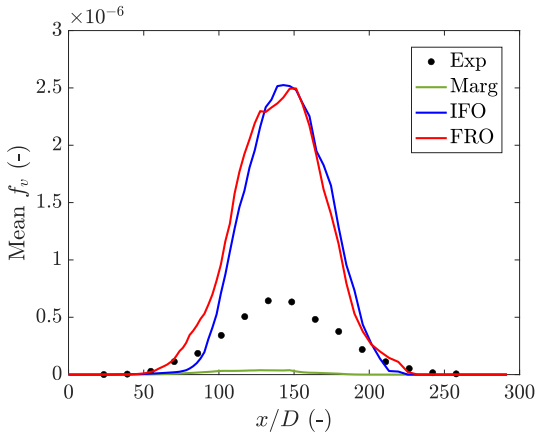

Figure 10: Mean soot volume fraction profiles along the centerline in the Sandia burner. Comparison of computational results using the three soot subfilter PDF models and experimental measurements from Ref. [30].

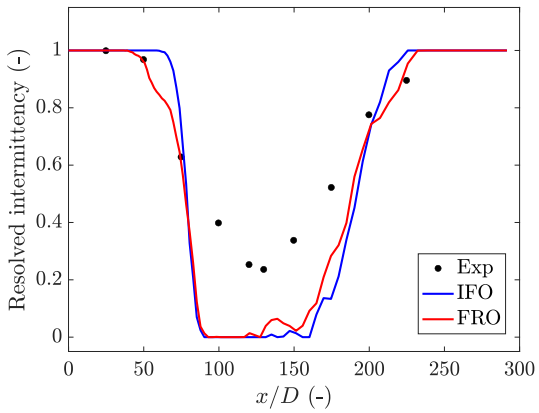

Figure 11: Soot resolved intermittency along the centerline in the Sandia burner. Comparison of computational results using the IFO and FRO soot subfilter PDF models and experimental measurements from Ref. [30].

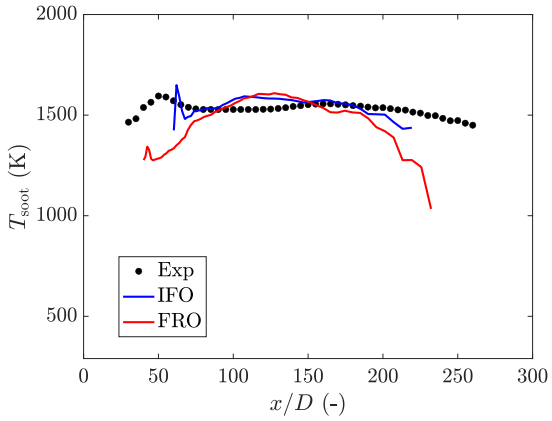

Figure 12: Soot temperature along the centerline in the Sandia burner. Comparison of computational results using the IFO and FRO soot subfilter PDF models and experimental measurements [17].

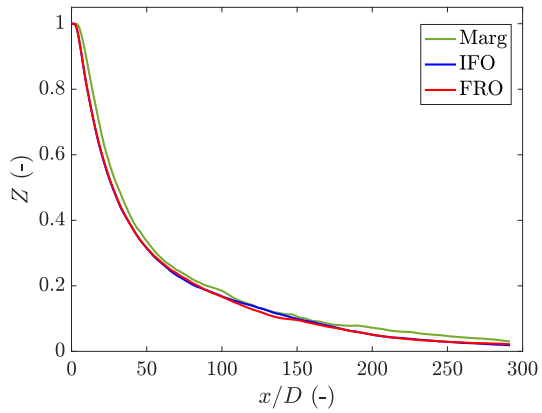

Figure 13: Mean mixture fraction along the centerline in the Sandia burner: soot subfilter PDF models do not affect the mixture processes.

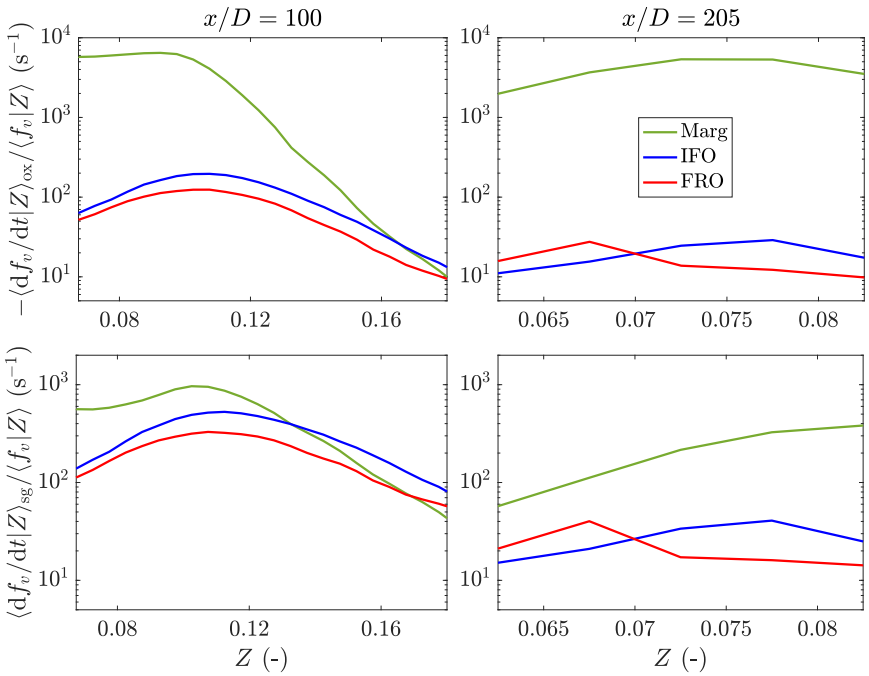

Figure 14: Profiles of normalized conditional mean soot volume fraction source terms $\langle \mathrm{d}f_v/\mathrm{d}t \mid Z\rangle/\langle f_v \mid Z\rangle$ in mixture fraction Z, for oxidation (magnitude, top) and surface growth (bottom), and at two different positions above the Sandia burner: $x/D = 100$ (left) and $x/D = 205$. Comparison of computational results using the three soot subfilter PDF models.

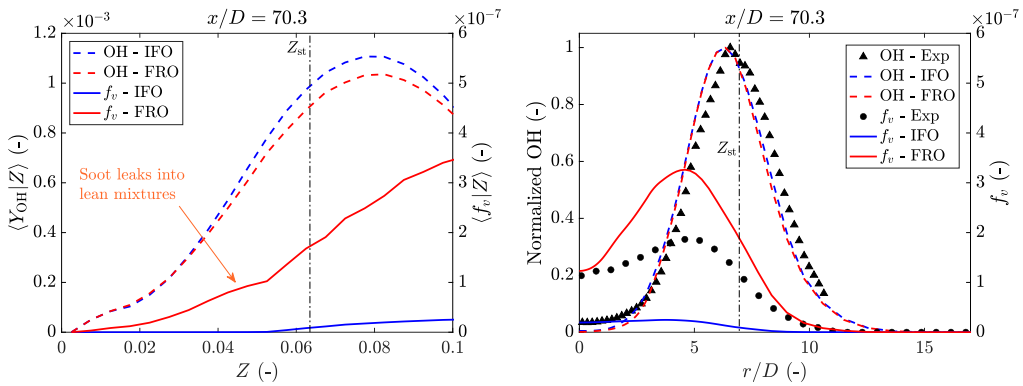

Figure 15: Left: conditional mean OH mass fraction $\langle Y_{\mathrm{OH}} \mid Z\rangle$ and soot volume fraction $\langle f_v | Z\rangle$ profiles in mixture fraction Z. The stoichiometric mixture is also indicated (vertical line). Right: Radial profiles of normalized OH mass fraction and mean soot volume fraction f_v. Comparison of computational results using the IFO and FRO soot subfilter PDF models and experimental measurements [17, 30] at $x/D = 70.3$. The vertical line indicates the spatial position where $\langle Z\rangle = Z_{\mathrm{st}}$.